Azimuth Cutoff Compensation Method for SAR Wave Observation Based on Multiview Wave Spectrum Data Fusion

YONG WAN[ID], XIAOYU ZHANG, YONGSHOU DAI, LIGANG LI, AND XIAOJUN QU

College of Oceanography and Space Informatics, China University of Petroleum, Qingdao 266580, China

Corresponding author: Yong Wan (wanyong@upc.edu.cn)

ABSTRACT Azimuth cutoff is an inherent disadvantage of synthetic aperture radar (SAR) waves observation. The waves shorter than some certain wavelength (azimuth cutoff) cannot be imaged in original form (structures) by SAR. For a single SAR observation, the problem of the azimuth cutoff for ocean waves can be resolved to some extent by cooperative observations of SAR satellites. Multiple SAR satellites are required to achieve simultaneous observation of an ocean area to obtain multiview SAR ocean wave synchronization data. Currently, these data cannot be acquired from in-orbit SARs. In this study, imaging simulations of multiview SAR ocean wave synchronization data based on small SAR satellites were carried out for the first time with X-band, 4-m resolution, stripmap mode and Single Look Complex (SLC) product. The Max Planck Institute (MPI) method was used to obtain the optimum wave spectrum of the synchronous data. The influencing factors of the azimuth cutoff wavelength were analyzed by using measured and simulated SAR data. The analysis results were used to develop a novel multiview wave spectrum data fusion method for azimuth cutoff compensation. The azimuth cutoff compensation effect was evaluated by comparing the inversion results before and after data fusion: the azimuth cutoff decreased by 9.76% on average, the root mean square error (RMSE) of the significant wave height is 0.06m, and RMSE of the mean wave period is 0.58s. The azimuth cutoff compensation method can be applied to SAR data for medium and low sea states (that is, wind speeds of 5-15 m/s). These results show that the proposed method of multiview wave spectrum data fusion effectively compensates for azimuth cutoff.

INDEX TERMS Multiview SAR wave synchronization data, wave spectrum data fusion, azimuth cutoff wavelength compensation.

I. INTRODUCTION

Ocean waves are typically generated by local winds and can be categorized as wind sea waves and swells. Additional sources of wave generation are tides, currents, internal waves, thalassogenic movement, changes in atmospheric pressure, the uneven distribution of seawater density, etc. The mechanism of the formation and evolution of ocean waves has become an important research field in oceanography. Synthetic aperture radar (SAR) is an effective means of observing large areas of ocean waves to obtain a two-dimensional (2D) ocean wave spectrum [1]. In addition, recently the X-band radar are also widely used on wave observation [2], [3]. Compared with other remote sensing methods, such as altimetry and wave spectrometry, SAR has

The associate editor coordinating the review of this manuscript and approving it for publication was Weimin Huang[ID].

very high spatial resolution, the observation results are not affected by near-shore terrain, and fine detection is possible for a wide range of waves. All SAR-wave methods are divided in two categories: using spectra transform and empirical algorithms without this transform allow estimating practically all sea state integrated parameters accurately, fast and in fields for all images without excluding "bad images" and which allows to use them for Near Real Time Services (NRT) [4]. Alpers [5] and Hasselmann [6] performed detailed studies showing three main modulation mechanisms in SAR wave imaging: tilt modulation, hydrodynamic modulation, and velocity bunching modulation. However, nonlinear effects from velocity bunching modulation in the azimuth direction limit SAR imaging to wave structures with wavelengths above a defined threshold. This threshold is called the azimuth cutoff wavelength, or simply, the azimuth cutoff which will affect the wave measurement accuracy. In addition

to azimuth cutoff, there are also other factors that negatively affect the wave measurement accuracy using radars operating at X-band, such as precipitation [7], [8].

The factors that affect the azimuth cutoff include the range-velocity ratio [9], the significant wave height [11]–[13], the wind speed, the wave orbital velocity [13] etc. Hasselmann *et al.* [19] analyzed the relationship between the azimuth cutoff wavelength and the modulation transfer function. G. Grieco et al used ERS-1 and Sentinel-1 measured data to correlate the azimuth cutoff, wind speed and significant wave height. Corcione et al proposed an azimuth cutoff implementation method to retrieve the ocean surface wind speed from SAR imaging measurements. Li et al used quad-polarized Radarsat-2 and Gaofen-3 products to analyze the dependence of the azimuth cutoff on the polarization and the incidence angle. Most of the abovementioned studies involve the mutually dependent estimation of the azimuth cutoff and wave parameters. No studies have been performed on eliminating and compensating for the influence of the azimuth cutoff. The objective of this study is azimuth cutoff compensation. For this purpose, multiview SAR wave synchronization data were acquired from cooperative satellite observations. In the literature, Lyzenga and Malinas et al presented a prototype for azimuth compensation, wherein the azimuth cutoff was corrected by measuring a wave spectrum using dual-antenna SAR. The authors suggested that the azimuth cutoff effect could be compensated using two SAR satellites.

At present, in-orbit satellites cannot be used to realize simultaneous observation of an ocean area in different observation directions or obtain multiview synchronization data. Therefore, multiview synchronization data can only be obtained from imaging simulations. Most existing imaging simulations involve a single SAR, and synchronous imaging simulations of multiple SARs have not been performed. In the present study, single SAR imaging simulations were used to carry out an imaging simulation of networked satellites with three SARs, thereby simulating multiview SAR wave synchronization data. Ocean SAR images were indirectly obtained by simulating the generation of SAR echo signals, which has the advantages of being independent of the imaging model and producing very accurate imaging results [18].

The SAR wave synchronization data (refers to collocated data acquired by multiple SAR satellites observing the same ocean area simultaneously in different observation directions) were then inverted. The transformation from the wave spectrum to the SAR image spectrum is nonlinear. Researchers have proposed a variety of SAR wave spectrum inversion methods. Hasselmann *et al.* deduced a nonlinear transformation from the wave direction spectrum to the SAR image spectrum, which was used to develop the Max Planck Institute (MPI) algorithm, the earliest proposed wave spectrum inversion algorithm. In 1996, Hasselmann *et al.* improved the MPI algorithm, which became the basis of other inversion methods. The MPI algorithm produces relatively accurate

inversion results and is therefore used in the present study to invert the synchronous ocean wave spectrum.

This paper is structured as follows. In Section II, the basic principles of the SAR imaging simulation and the MPI algorithm are introduced. In Section III, the estimation of the azimuth cutoff and the data fusion method are described. Section IV is an analysis of the results obtained in this paper. Conclusions are provided in the final section.

II. METHODS
A. SIMULATION OF MULTIVIEW SAR WAVE SYNCHRONIZATION DATA
The simulation of multiview SAR wave synchronization data consists of the following steps: simulation of the wave spectrum, simulation of the ocean surface, calculation of the backscattering coefficient, generation of echo signals, SAR imaging of ocean waves, and synchronization of the ocean wave data [20], [21].

1) WAVE SPECTRUM SIMULATION
In this study, the Elfouhaily spectrum [22] was adopted to simulate the time-varying ocean surface. The Elfouhaily spectrum is a complete wavenumber spectrum based on the low-wavenumber Jonswap spectrum and the high-wavenumber Phillips spectrum [23] and is highly representative of the actual sea state. A key feature of the Elfouhaily spectrum is that high and low wavenumbers are modeled similarly. The direction function of the spectrum is symmetric with respect to the wind direction and is correlated with the wavenumber and the wind speed. The low-wavenumber component of the Elfouhaily spectrum is expressed as

$$B_l = \frac{\alpha_p}{2} \cdot \frac{c_p}{c} \cdot F_p, \quad (1)$$

where α_p is the equilibrium range parameter for long waves, c_p is the phase velocity corresponding to the peak wavenumber, c is the speed of light and F_p is the longwave side effect function. The high-wavenumber component of the Elfouhaily spectrum is expressed as

$$B_h = \frac{\alpha_m}{2} \cdot \frac{c_m}{c} \cdot F_m, \quad (2)$$

where α_m is the equilibrium range parameter for short waves, c_m is the minimum phase velocity, and F_m is the shortwave side effect function. The full wavenumber spectrum is given by

$$S = k^{-3}(B_l + B_h) \quad (3)$$

The direction function formula is as follows:

$$f(k, \varphi) = [1 + \Delta(k)\cos(2\varphi)]/2\pi. \quad (4)$$

The wavenumber direction spectrum can be represented in terms of the wavenumber spectrum and the direction function as follows:

$$E(k, \varphi) = S \cdot f(k, \varphi)/k. \quad (5)$$

where φ represents the wave propagation direction.

2) OCEAN SURFACE SIMULATION

After the wave spectrum simulation is completed, a linear filtering method is used to simulate the 2D ocean surface. 2D Gaussian white noise is generated in the frequency domain and linearly filtered by the wave spectrum. An inverse Fourier transform (IFFT) is performed to obtain the ocean surface height distribution [24].

Performing an IFFT on $A_L(\vec{k}, t)$ generates a linear ocean surface as follows:

$$\eta_L(\vec{r}, t) = \frac{1}{L_x L_y} \sum \sum A_L(\vec{k}, t) \exp(i\vec{k} \cdot \vec{r}), \quad (6)$$

where $\eta_L(\vec{r}, t)$ represents the ocean surface height at time t and position $\vec{r}$, A_L represents the Fourier transform of the sea level fluctuation function. The following relationship must be satisfied for η_L to be real:

$$A_L(k_x, k_y) = A_L^*(-k_x, -k_y)$$
$$A_L(k_x, -k_y) = A_L^*(-k_x, k_y). \quad (7)$$

3) CALCULATION OF BACKSCATTERING COEFFICIENT

The typical SAR incidence angle range is 20°-60°. A SAR electromagnetic wave exhibits medium-range resonance scattering with the ocean surface. Bragg scattering causes ocean surface backscattering [25]. Therefore, the accuracy of the backscattering coefficient determines the accuracy of the SAR imaging data. In this study, a two-scale electromagnetic scattering model is used to calculate the backscattering coefficient for a VV SAR polarization mode. The backscattering coefficient can be expressed as [26]

$$\sigma_{BVV}^0(\theta) = 8k^4 \cos^4 \theta |U_{VV}|^2 S(2k \sin \theta, 0)$$
$$U_{VV} = \frac{(\varepsilon - 1)[\sin^2 \theta - \varepsilon(1 + \sin^2 \theta)]}{[\varepsilon \cos \theta + \sqrt{\varepsilon - \sin^2 \theta}]^2}, \quad (8)$$

where θ is the SAR incidence angle, k is the number of electromagnetic waves emitted by the SAR, ε stands for seawater dielectric constant and U_{VV} is the vertical polarization factor.

4) GENERATION OF ECHO SIGNALS

The echo signals are simulated using a time-domain algorithm and a frequency-domain algorithm. The time-domain algorithm simulates the actual SAR working process and acquires the original echo signals. Although a large amount of computation is required, very accurate echo signals are generated. The echoes of K point targets can be obtained by superposition, as shown in equation (9). Point targets have zero height. Thus, the finite height of the simulated ocean surface is incorporated into the calculation of the echo signals as follows:

$$Sr(n, m)$$
$$= \sum_{k=1}^{K} \sigma \cdot \exp\{j\pi [t(m) - \frac{2R(n;k)}{C}]\} \cdot \exp[-j\frac{4\pi}{\lambda} R(n;k)]$$
$$0 < [t(m) - \frac{2R(n;k)}{C}] < Tr; |R(n;k) - x(k)|$$
$$< Tsar \quad n = 1, 2, 3 \ldots N; m = 1, 2, 3 \ldots M, \quad (9)$$

TABLE 1. System parameters.

Parameters	Value	Parameters	Value
Platform height	530 km	Orbital semimajor axis	6901 km
Speed	7600 m/s	Orbital flattening	0.003
Observation angle of incidence	30°	Orbital inclination	97.423°
Carrier frequency	9.5 GHz	Right ascension	60
Pulse duration	10 μs	Perigee amplitude angle	160
Chirp frequency modulation bandwidth	100 MHz	Moment of flight ascending node	0

where C is the speed of light, σ is the backscattering coefficient, $R(n; k)$ is the slant distance, $Tsar$ is the SAR integration time, and Tr is the pulse duration. n and m represent the number of imaging points in azimuth and range direction respectively.

5) SIMULATION OF SYNCHRONIZATION DATA

The range-Doppler (RD) imaging algorithm processes the echo signals to produce ocean surface SAR images. The SAR that implements the imaging simulation is denoted by SAR-1. Based on the parameters and working principle of SAR-1, two other SARs, SAR-2 and SAR-3, are simulated at 10° and 20° to the SAR-1 flight direction, respectively. The SAR-2 and SAR-3 orbits are obtained by counterclockwise rotation of the SAR-1 orbit. The satellites are simulated by neglecting the Earth's rotation and ground bending. It is challenging to adjust the position coordinates of the subsatellite points according to the SAR orbital parameters to produce the angles between the tracks of the three SARs. The three SARs operate as a satellite network, enabling simultaneous observation of an ocean area and synchronization of SAR ocean wave data. Some of the SAR system parameters are shown in Table 1.

B. MPI WAVE SPECTRUM INVERSION METHOD

SAR imaging of swells can generally be linearly approximated. But this statement does not match the whole reality such as for TerraSAR-X and Sentinel-1 some swell parameters are not more correct imaged by wave height over some values. However, nonlinearity is a significant characteristic of wind waves. Hasselmann derived the following nonlinear transformation between the SAR image spectrum and the wave direction spectrum:

$$P^S(k) = \frac{1}{4\pi^2} \exp(-k_x^2 \xi'^2) \cdot \int \exp(-k_x^2 \xi'^2 \langle v^2 \rangle^{-1} f^v(\mathrm{r}))$$
$$\cdot \{1 + f^R(\mathrm{r}) + ik_x \beta(f^{Rv}(\mathrm{r}) - f^{Rv}(-\mathrm{r}))$$
$$+ k_x^2 \beta^2 [f^{Rv}(\mathrm{r}) - f^{Rv}(0)][f^{Rv}(-\mathrm{r}) - f^{Rv}(0)]\} d\mathrm{r} e^{-ikr}, \quad (10)$$

where

$$f^R(r) = 0.5 \int \frac{(F(k)|T_k^R|^2}{+F(-k)|T_{-k}^R|^2)} \exp(ikr)dk \quad (11)$$

$$f^v(r) = \int F(k)|T_k^v|^2 \exp(ikr)dk \quad (12)$$

$$f^{Rv}(r) = 0.5 \int \frac{(F(k)T_k^R(T_k^v)^*}{+F(-k)T_{-k}^v(T_{-k}^R)^*)} \exp(ikr)dk. \quad (13)$$
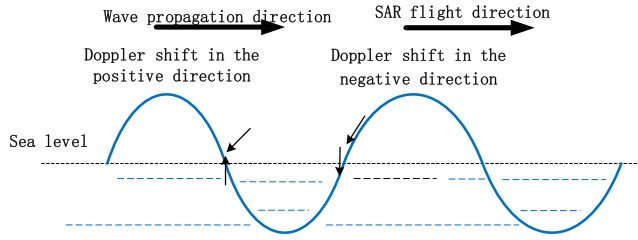
FIGURE 1. Schematic of velocity bunching modulation.

Equations (11) and (12) correspond to the autocorrelations of the SAR image intensity and the velocity along the track direction, respectively. Equation (13) is the correlation of these two correlations. The MPI algorithm for inverting the wave spectrum derives from this nonlinear transformation. This algorithm maps the ocean wave spectrum to the SAR image spectrum. Information loss in the inversion process from the 180° mapping ambiguity and azimuth cutoff must be prevented. The algorithm introduces a first-guess wave spectrum and constructs a value function. The value function is minimized through iteration, and the optimum wave spectrum and the optimum SAR spectrum are outputted.

III. ESTIMATION OF AZIMUTH CUTOFF AND WAVE SPECTRUM DATA FUSION METHOD

A. ESTIMATION OF AZIMUTH CUTOFF AND ANALYSIS OF INFLUENCING FACTORS

In fact, as moving dynamic targets, the waves shorter than some certain wavelength (azimuth cutoff) cannot be imaged in original form (structures) by SAR. The nonlinear effect of velocity bunching modulation is the main cause of the azimuth cutoff. This nonlinearity is speed-dependent: if the image displacement is small relative to the wavelength, the velocity bunching modulation has a linear effect. However, the effect is nonlinear if the displacement of the facets is equal to or greater than the wavelength. This nonlinear modulation applies only to waves propagating in the azimuth direction, because SAR achieves high azimuthal resolution through the synthetic aperture in azimuth and in-range pulse compression, whereas the principle of synthetic aperture is based on the Doppler effect. The velocity bunching modulation process is shown in Figure 1. When a wave propagates in the azimuth direction, the area in front of the crest produces an additional upward velocity, resulting in a positive Doppler shift. The scattering target moves in the positive direction of the azimuth in the SAR image, and the scattering bins gather near the trough, making the trough brighter and the crest darker. If a downward additional velocity is generated behind the wave peak, the scattering target moves in the negative direction of the azimuth in the SAR image. The SAR wave image will have a darker trough and a brighter crest. The magnitude of the displacement is d $= \beta^* u_r$, where β is the range-to-velocity ratio, and ur is the radial velocity component toward the radar. This displacement causes blurring of the SAR image in the azimuth direction, and wave information below the azimuth cutoff

is lost. There is an additional mechanism for azimuth cutoff. The limited scatterer time results in a coherence time of the wave scene below the SAR acquisition time T, which leads to the following azimuth cutoff:

$$T = \frac{R\mu}{V_f}, \tag{14}$$

where R denotes the slant range of the SAR to the imaging target, μ denotes the azimuth beamwidth of the antenna pattern; and V_f denotes the antenna pattern footprint velocity across the Earth's surface for spaceborne SAR and is the same speed as the platform velocity in orbit for airborne SAR [19].

The well-known cutoff effect has been explained in terms of velocity bunching based on SAR images from satellites with specific bands and resolution. However, a series of SAR images from newer satellites, e.g., TerraSAR (X-band) with low altitudes of 500 km and high resolution up to 1 m, contradict this explanation. The strongest impact on nonlinear effects appears to result from the radial component of the phase velocity of the wave crest instead of the local orbital wave velocity. Therefore, the reason for the azimuth cutoff effect varies among different SAR satellites [29].

In the absence of a closed form expression, the azimuth cutoff must be estimated. Beal was the first to propose an empirical formula for the azimuth cutoff in 1983 using the range-to-velocity ratio and the significant wave height. However, the wind speed, wave orbital velocity, etc., also affect the azimuth cutoff. A variety of methods for estimating the azimuth cutoff have since emerged. In this study, equation (15) is used to estimate the azimuth cutoff. This method is based on the hypothesis of linear waves [17] and considering the line-of-sight orbital velocity rather than the vertical velocity [10]:

$$()\lambda_{\mathrm{c}} = \pi\beta\sqrt{\int |T_k^v|^2 F(k)\mathrm{d}k}, \tag{15}$$

where

$$T_k^v = -\omega(\sin\theta\frac{k_r}{|k|} + \mathrm{i}\cdot\cos\theta) \tag{16}$$

$$\cos\varphi = \frac{k_r}{|k|}, \tag{17}$$

where ω is the angular frequency, θ is the SAR incidence angle, k_r is the component of the wavenumber in the range direction, k is the wavenumber, and T_k^v is the range velocity transfer function. Inversion using the MPI algorithm produces the optimum wave spectrum $S(k)$.

The azimuth cutoff is related to the significant wave height, the wind speed, the range-to-velocity ratio, θ, and the wave propagation direction. In this study, processed 24 ENVISAT ASAR and Radarsat-2 measured data were used to determine the relationship between the wave parameters and the azimuth cutoff. The basic information of the 24-scene data is shown in Table 2. The variables included in the SAR data were the significant wave height, the wind speed, the wavenumber spectrum, etc.

TABLE 2. Information from 24-scene SAR measured data.

SAR data label	Time	Latitude and longitude range	SAR data label	Time	Latitude and longitude range
ASA_IMS_1PNDPA20101012 _021940_000000162093_0040 4_45047_0301	2010.10.12 02:19:48	38.9°N–40.1°N 118.5°E–120.1°E	RS2_OK29469_PK291175 _DK265287_S5_20120504 _215847_VV_VH_SLC	2012.05.04 21:58:55	37.3503° N–38.4314°N 120.1911°E–121.6256°E
ASA_IMS_1PNDPA20101012 _021953_000000162093_0040 4_45047_0294	2010.10.12 02:20:01	38.15°N–39.33°N 118.38°E–119.86°E	RS2_OK29469_PK291177 _DK265289_S5_20120507 _095633_VV_VH_SLC	2012.05.07 09:56:41	37.3622°N–38.4428°N 120.2247°E–121.6606°E
ASA_IMS_1PNDPA20101012 _022007_000000162093_0040 4_45047_0295	2010.10.12 02:20:15	37.3947°N–38.4869°N 120.2619°E–121.705°E	RS2_OK29469_PK291174 _DK262913_S5_20120430 _100011_VV_VH_SLC	2012.4.30 10:00:19	35.4572° N–36.5403°N 119.6169°E–121.0189°E
ASA_IMS_1PNIPA20110730_ 021919_000000163105_00075 _49227_0084	2011.07.30 02:19:27	37.31°N–38.49°N 118.16°E–119.62°E	RS2_OK29469_PK291176 _DK265288_S5_20120504 _215921_VV_VH_SLC	2012.05.04 21:59:29	35.3692°N–36.4517°N 119.7708°E–121.1697°E
ASA_IMS_1PNIPA20110730_ 021933_000000163105_00075 _49227_0083	2011.07.30 02:19:41	38.01°N – 39.12°N 118.38°E–119.54°E	RS2_OK29469_PK291178 _DK265290_S1_20120507 _221148_VV_VH_SLC	2012.05.07 22:11:56	35.4125°N- 36.5097°N 119.51°E -120.8597°E
ASA_IMS_1PNUPA20090419 _133817_000000162078_0018 2_37310_0161	2009.04.19 13:38:25	37.5°N–38.68°N 120.59°E–122.06°E	RS2_OK29469_PK292895 _DK262912_S3_20120427 _220329_VV_VH_SLC	2012.04.27 22:03:37	35.3244°N–36.4175°N 119.7908°E–121.1953°E
ASA_IMS_1PNUPA20090419 _133831_000000162078_0018 2_37310_0173	2009.04.19 13:38;39	38.33°N– 39.51°N 120.35°E–121.84°E	RS2_OK31199_PK310675 _DK277122_S3_20120725 _095222_VV_SLC	2012.07.25 09:52:30	37.3694°N–38.4617°N 120.1681°E–121.6119°E
ASA_IMS_1PNUPA20090419 _133845_000000152078_0018 2_37310_0158	2009.04.19 13:38:53	39.17°N– 40.31°N 120.12°E–121.61°E	RS2_OK31199_PK310676 _DK277123_S4_20120727 _224826_VV_SLC	2012.07.27 22:48:33	37.45°N–38.6417°N 120.2178°E–121.7642° E
ASA_IMS_1PNUPA20100118 _021109_000000162086_0008 9_41225_0165	2010.01.18 02:11:18	39.1°N– 40.27°N 120.14°E- 121.61°E	RS2_OK31199_PK310677 _DK277124_S2_20120801 _094812_VV_SLC	2012.08.01 09:48:21	37.345°N–38.2531°N 120.075°E–121.5333°E
ASA_IMS_1PNUPA20100118 _021124_000000162086_0008 9_41225_0166	2010.01.18 02:11:32	38.26°N– 39.43°N 119.92°E–121.38°E	RS2_OK31198_PK310678 _DK277125_S2_20120725 _220739_VV_SLC	2012.07.25 22:07:47	35.2486°N–36.1567°N 119.8289°E–121.2444°E
ASA_IMS_1PNUPA20100118 _021138_000000162086_0008 9_41225_0167	2010.01.18 02:11:46	37.43°N–38.6°N 119.7°E–121.14°E	RS2_OK31198_PK310679 _DK277126_S3_20120801 _220330_VV_SLC	2012.08.01 22:03:38	35.2583°N–36.3514°N 119.7767°E–121.18°E
RS2_OK29469_PK291172_D K262911_S3_20120427_22025 4_VV_VH_SLC	2012.4.27 22:03:02	37.3947°N–38.4869°N 120.2619°E–121.705°E	RS2_OK31198_PK310931 _DK277277_S3_20120708 _220330_VV_SLC	2012.07.08 22:03:37	35.2592°N–36.3519°N 119.7761°E–121.1797°E

The ENVISAT ASAR data ASA_IMS_1PNIPA201107 30_021919_000000163105_00075_49227_0084.N1 is considered as an example: 10 small areas with clear wave information were selected, and the azimuth cutoff for each area was estimated. The SAR parameters, such as the SAR incidence angle, the platform velocity, and the platform height, were obtained. A schematic of the angle between the azimuth and north is shown in Figure 2. The horizontal and vertical axes in the figure are the range direction and the azimuth direction, respectively, and the black arrow points north. The parameters extracted from the data are shown in Table 3.

After the wave parameters were extracted from the 24-scene SAR data, linear regression was used to correlate the azimuth angle (the independent variable) and the azimuth cutoff (the dependent variable). The azimuth cutoff was found to be independent of the azimuth angle.

The results show that in this case, the real SAR data could not be used to correlate the azimuth cutoff and the azimuth angle because the factors affecting the azimuth cutoff, such as wind speed and significant wave height, were not consistent. Therefore, the simulated SAR data, wherein the wind speed was consistent, was used to correlate the
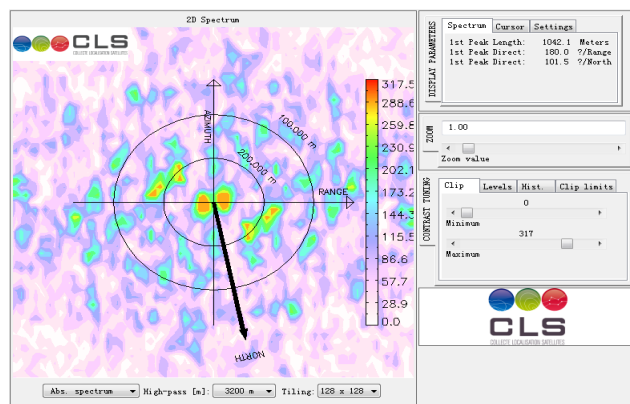
FIGURE 2. Schematic showing orientation between azimuth and north.

azimuth cutoff and the azimuth angle and is discussed in the next section.

B. WAVE SPECTRUM DATA FUSION METHOD

In this study, the wave data fusion method was used to compensate the SAR wave azimuth cutoff. First, the MPI method was used to extract a single SAR wave spectrum, and the azimuth angle was correlated with the azimuth cutoff.
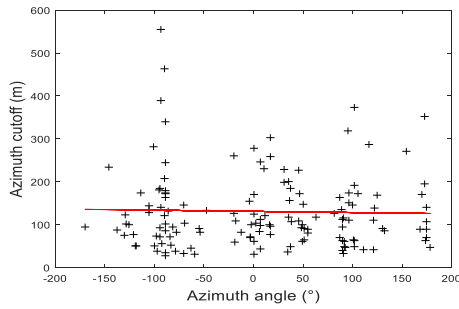
FIGURE 3. Result obtained from fitting azimuth cutoff to azimuth angle for real SAR data.

TABLE 3. Various parameters extracted from ASAR data.

Azimuth cutoff (m)	Significant wave height (m)	Wind speed (m/s)	SAR incident angle (°)
120.931	0.82	6.047	26.5971
101.462	0.8	4.386	26.2916
173.2293	1.158	4.15	27.2147
389.6311	3.6	7.52	28.0946
171.206	1.31	5.036	27.2159
555.6558	4.99	8.117	28.0958
100.6521	0.802	7.445	28.3843
50.0034	0.626	10.536	26.3098
126.604	1.519	11.531	28.1058
174.2902	1.36	12.58	28.3887
Wave propagation direction (°)	Angle between azimuth and north (°)	Azimuth angle (°)	
180		11.5	
280		-88.5	
280		-88.5	
285		-93.5	
280	168.5	-88.5	
285		-93.5	
320		-128.5	
310		-118.5	
200		-20	
95		96.5	

This correlation was used to formulate a multiview wave spectrum data fusion method. The multiview wave spectrum data were fused to compensate the azimuth cutoff, and the compensation effect was verified. Thus, the azimuth cutoff compensation method was based on wave data fusion. Before establishing the wave spectrum data fusion method, the influence of different wave propagation directions on the azimuth cutoff should be investigated. Wave propagation at an angle to the SAR flight direction (the azimuth direction) affects the intensity of the azimuth cutoff of the SAR observation wave. Claus has shown that in a strongly nonlinear imaging scheme, the velocity bunching mechanism causes the peaks to rotate toward the range direction [30]. The highest nonlinear imaging distortion was found for broad spectra (wind waves) and weak for narrowband swells. In linear and weakly nonlinear imaging schemes, the superposition of hydrodynamic and tilt cross-section modulations with a velocity bunching transfer function typically produced a rotation of the spectral peak toward the azimuthal direction. The interference characteristics of different modulation mechanisms depend on the wave
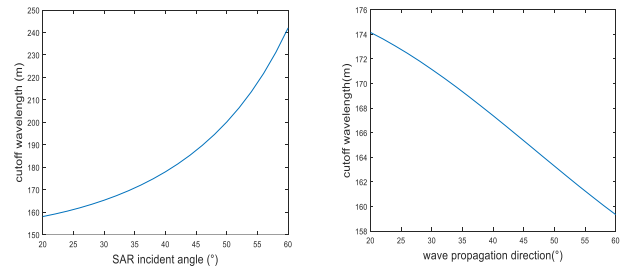

FIGURE 4. (a) Relationship between azimuth cutoff and incident angle and (b) relationship between azimuth cutoff and φ_0.

TABLE 4. Azimuth cutoff and azimuth angle for different SAR data.

Azimuth cutoff (m)	Azimuth angle (°)	Azimuth cutoff (m)	Azimuth angle (°)
156.95	45°	161.54	95°
158.56	55°	160.99	105°
159.96	65°	159.96	115°
160.99	75°	158.56	125°
161.54	85°	156.95	135°

propagation direction, which was shown to be an important factor affecting the azimuth cutoff. Therefore, the relationship between the azimuth angle and the azimuth cutoff formed the basis for the multiview SAR wave spectrum data fusion method.

The simulated SAR data were then used to correlate the azimuth cutoff and the azimuth angle. The E-spectrum simulated data were used as $S(k)$. Equation (18) shows that for fixed parameters, such as φ_0 and the range-to-velocity ratio, the azimuth cutoff increases with the SAR incidence angle θ, as shown in Figure 4(a). Fixing θ and varying only φ_0 shows that the larger φ_0 is, the smaller the azimuth cutoff value is, as shown in Figure 4(b). As the azimuth angle and φ_0 are mutually dependent, it can be inferred that, for acute azimuth angles, the azimuth angle is proportional to the azimuth cutoff. All angles are defined relative to the positive azimuth and range directions.

To consider obtuse azimuth angles, we simulated SAR data at different azimuth angles and calculated the corresponding azimuth cutoff wavelengths, as shown in the following table.

These results show that for acute azimuth angles, the azimuth cutoff wavelengths are proportional to the azimuth angles. However, for obtuse azimuth angles, the azimuth cutoff wavelengths are inversely proportional to the azimuth angles. This result can be explained by considering the properties of the cosine function in equations (15)-(17). As two complementary numbers have the same absolute cosine values, complementary azimuth angles have the same azimuth cutoff values. This consideration was used to establish a wave data fusion method. The steps of the method are shown in Figure 5 and outlined below.

(1) The azimuth angle for each single SAR is calculated.

(2) Data fusion weights are determined for different azimuth angles.

(3) The wave spectrum is obtained by inversion of a single SAR and divided into small units according to the
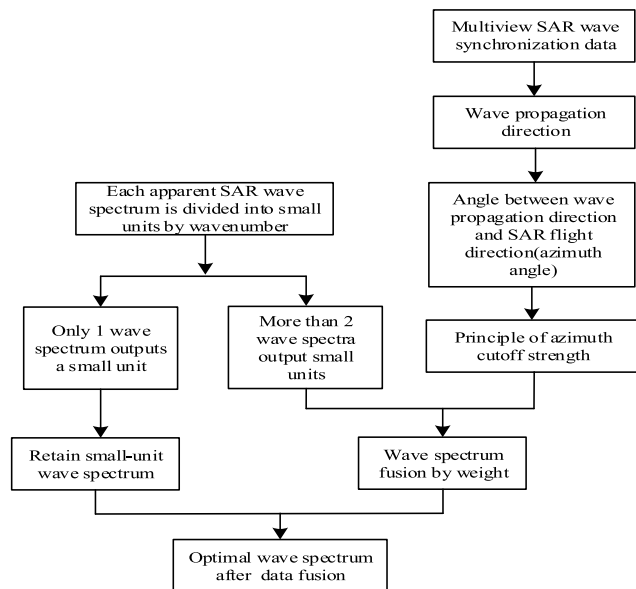
FIGURE 5. Flow chart of wave spectrum data fusion method.

wavenumber interval of the azimuth direction and the range direction. If a small unit has only 1 wave spectra output, the output of the small unit is retained; if a small unit has more than 2 wave spectrum outputs, the output wave spectrum is fused using the determined wave spectrum fusion weights.

Since the wave spectrum are not completely independent, the fusion weights are determined such that the sum of the weights is less than 1. Considering that the azimuth cutoff decreases with the azimuth angle, the fusion weights are determined based on quadrants. When the sum of the azimuth angles is in the 90°-180° range, the fusion weight is obtained by dividing the azimuth angle by 180°. When the sum of azimuth angles is in the 180°-270° range, if the azimuth angles are inversely proportional to the azimuth cutoff wavelengths, the fusion weights are obtained by dividing 270° by the azimuth angle based on the principle of inverse distance weighting. Similarly, when the sum of the azimuth angles is in the range of 270°-360° range, the azimuth angles are obtuse angle, and the azimuth angles are inversely proportional to the azimuth cutoff wavelengths: thus, the fusion weight is obtained by dividing 360° by the azimuth angle. After determining the fusion weight, the MPI algorithm was used to invert the SAR wave data, and the wave spectrum were merged to estimate the azimuth cutoff before and after fusion.

IV. RESULTS AND DISCUSSION

A. RESULTS OF MULTIVIEW SAR WAVE SYNCHRONIZATION DATA

The ocean surface simulation can be used to create a background field to calculate the backscattering coefficient. When the background field is constructed, the simulated SAR can emit electromagnetic waves and receive echoes. The backscattering coefficient is calculated from the electromagnetic scattering model. Therefore, the accuracy of the
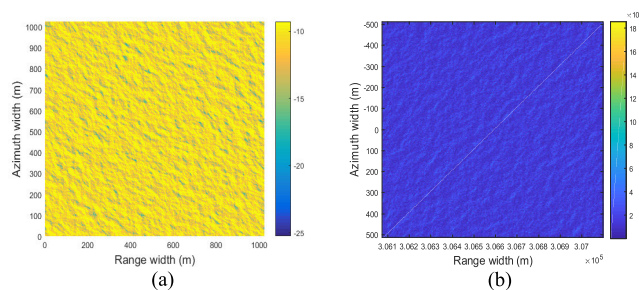

FIGURE 6. SAR-1 data: (a) backscattering coefficient and (b) SAR ocean image.
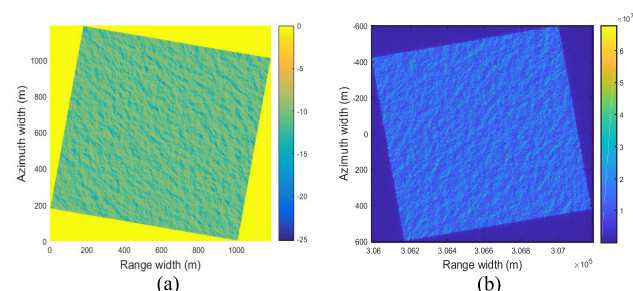

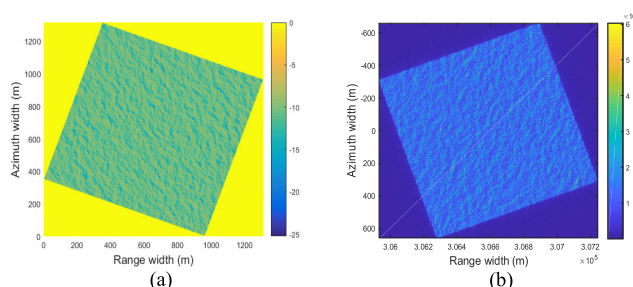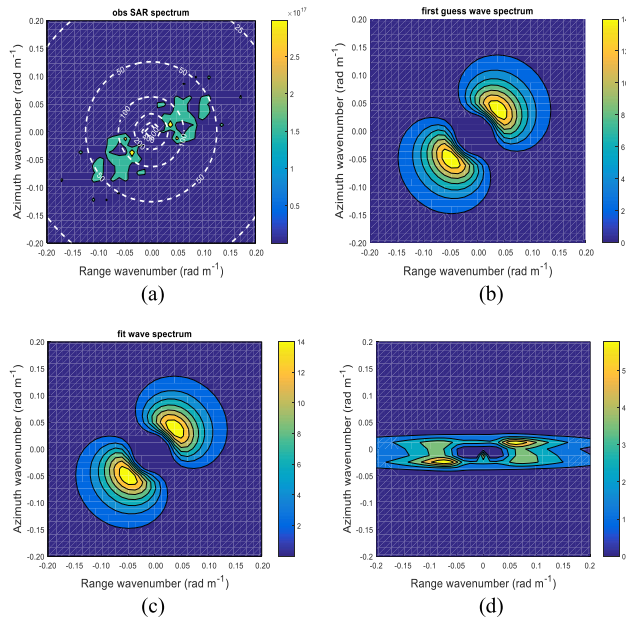FIGURE 7. SAR-2 data: (a) backscattering coefficient and (b) SAR ocean image.

FIGURE 8. SAR-3 data: (a) backscattering coefficient and (b) SAR ocean image.

constructed ocean surface directly determines the accuracy of the calculated backscattering coefficient. The FFT based linear filtering method has a rapid computation speed and produces clear ocean surface details. The 2D ocean surface simulated by the linear filtering method is the observation target. In this study, virtual networked satellites were simulated using three SARs, and networked cooperative observation was used to simulate the SAR synchronous observation data for different orbit directions. The backscattering coefficients obtained from the SAR observations and the corresponding ocean SAR images are shown in Figures 6-8.

The simulated ocean surface was used to calculate the backscattering coefficient, and the slope of the ocean surface was obtained to circumvent using the probability density function of an artificially assumed slope. In the figures, the backscattering coefficient of VV polarization typically ranges between −10 dB and −15 dB. The results in the figures are consistent with the literature [31], showing that the

FIGURE 9. SAR-1 wave spectrum inversion results: (a) observed SAR spectrum, (b) first-guess wave spectrum, (c) optimum wave spectrum, and (d) optimum SAR spectrum.

backscattering coefficient was accurately calculated. In the simulation process, the RD algorithm performed FFTs and IFFTs on the azimuth and range of the echo signals, respectively, which resulted in horizontal symmetry between the ocean SAR image and the backscattering coefficient.

B. WAVE SPECTRUM INVERSION OF SYNCHRONOUS DATA

After the multiview SAR synchronization data were simulated, the MPI algorithm was used to process the SAR wave data from the SAR-1 observations. The accuracy of the inversion results was used to verify the correctness of the simulated SAR data in Section IV.A. The inversion results of the SAR-1 acquired data are shown in Figure 9.

SAR-2 and SAR-1 had the same wave propagation direction of 45°. The orbital angle between SAR-1 and SAR-2 was 10°. As the included angle was obtained by a counterclockwise rotation, we inferred an included angle of 35° between the wave propagation direction and the SAR-2 range direction. The inversion results of the SAR-2 acquired data are shown in Figure 10.

The orbital angle between SAR-1 and SAR-3 was 20°, and the angle between the wave propagation direction and the range was calcuated to be 25°. The inversion results of the SAR-3 acquired data are shown in Figure 11.

Figures 9, 10, and 11 show that the first guess spectrum and the optimum wave spectrum have the same shape and magnitude. The value function shows that the closer the first guess spectrum was to the optimum wave spectrum, the more effective the inversion was. Note that the results of the observed SAR spectrum were obtained by horizontal inversion. The optimum SAR spectrum shows that the spectrum was compressed in the azimuth direction.
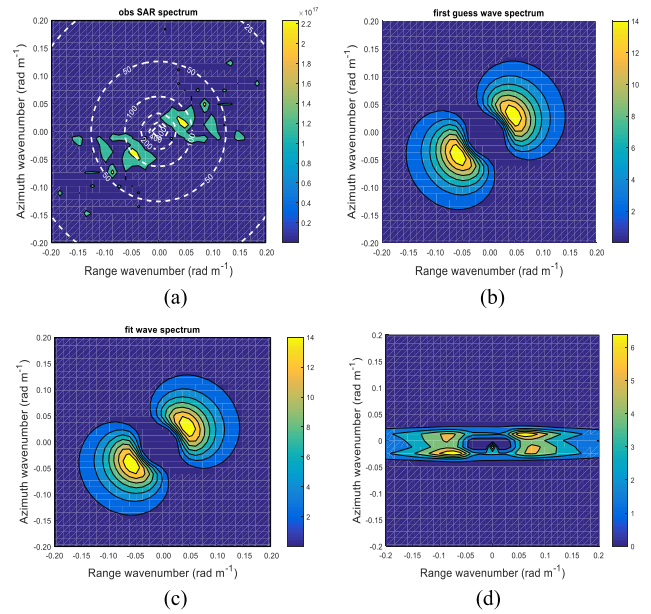
FIGURE 10. SAR-2 wave spectrum inversion results: (a) observed SAR spectrum, (b) first-guess wave spectrum, (c) optimum wave spectrum, and (d) optimum SAR spectrum.
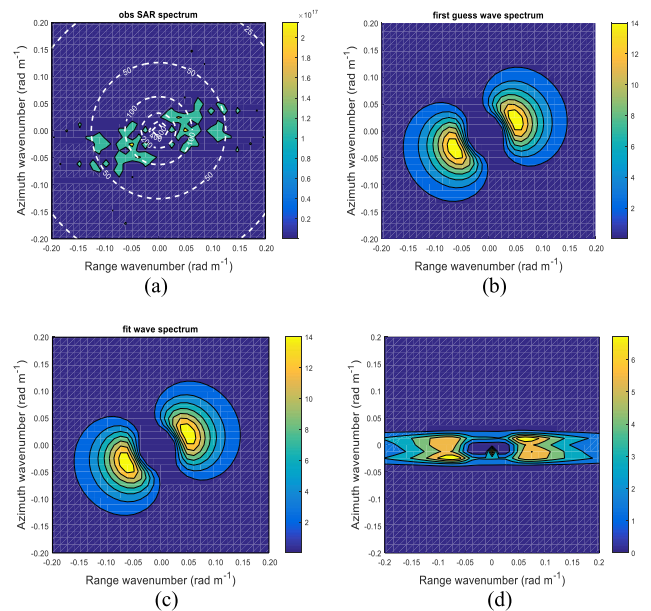
FIGURE 11. SAR-3 wave spectrum inversion results: (a) observed SAR spectrum, (b) first-guess wave spectrum, (c) optimum wave spectrum, and (d) optimum SAR spectrum.

Only waves with wavelengths larger than a defined threshold were imaged (that is, the high-wavenumber waves were truncated), which corresponded to the azimuth cutoff. The optimum SAR spectrum shows the influence of the azimuth cutoff on the SAR imaging.

C. SAR DATA WITH 0° AND 90° AZIMUTH ANGLES

The azimuth cutoff effect is generally considered to be strongest for waves in the azimuth direction and the weakest for waves in the range direction. Yoshida used numerical
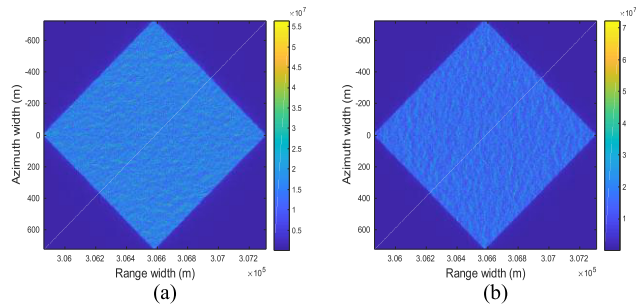
FIGURE 12. SAR data with azimuth angles of 0° and 90°.

simulations to study the effects of azimuth traveling waves and found that random displacements caused by the orbital motion of long waves produce false azimuth wave patterns [32]. Therefore, in this study, data with azimuth angles of 0° and 90° were simulated separately. The two types of SAR data represent wave propagation along the azimuth and range directions, respectively. When networked SARs observe the same sea area, the wave propagation direction is unchanged. Therefore, for a wave propagation direction of 45°, SARs with orbital angles of 45° and −45° to SAR-1 were simulated using SAR-1 as a reference. An SAR with an orbit angle of 45° corresponds to data with an azimuth angle of 90°, whereas an SAR with an orbit angle of −45° corresponds to data with an azimuth angle of 0°. The two new SARs are shown in Figure 12. The MPI method was used to invert the wave spectrum of the two types of SAR data, and the results are shown in the Figures 13-14.

The two types of SAR data represent waves propagating in the range and azimuth directions and can be regarded as special cases for azimuth cutoff compensation. The fusion weights were determined depending on the relevant subquadrant: for SAR data with an azimuth angle of 0°, the fusion weight was 0. Therefore, the SAR data with 0° azimuth angle did not participate in data fusion. Unfortunately, the proposed azimuth cutoff compensation method is not applicable to purely azimuthal traveling waves.

D. MULTIPLE-SAR SPECTRAL DATA FUSION AND AZIMUTH CUTOFF WAVELENGTH COMPENSATION

The obtained wave spectrum was fused using the established data fusion method. We established and verified the azimuth cutoff compensation method by simulating synchronous SAR data at 30°-70° (for 10°-intervals) to the SAR-1 orbit. The synchronous SAR data were classified into three groups for azimuth cutoff compensation: data at 10°-20° to the SAR-1 orbit and the SAR-1 data; data at 20°-40° to the SAR-1 orbit and the SAR-1 data; and data at 50°-70° to the SAR-1 orbit and the SAR-1 data. Thus, the SARs with acute azimuth angles were grouped separately from SARs with obtuse azimuth angles to prevent the azimuth angles from not being proportional to the azimuth cutoff wavelengths. In Table 4, the azimuth angles of the first group summed to 165°, so the fusion weights were the ratios between the azimuth angle and 180°. The fused formula is shown in equation (18).
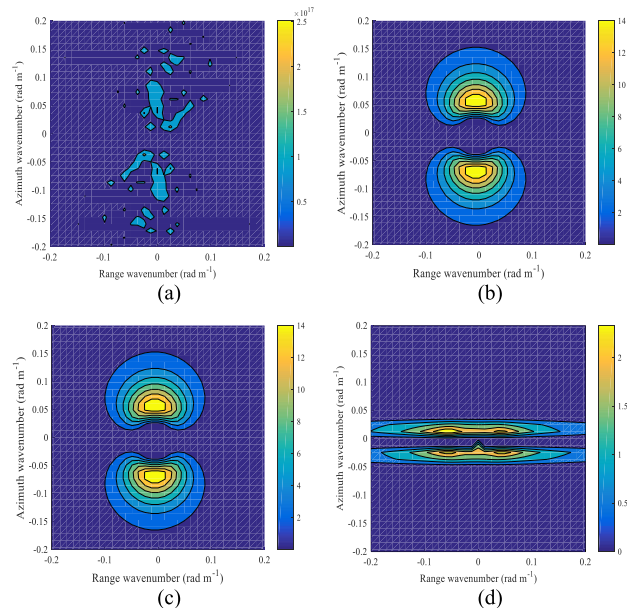

FIGURE 13. Wave spectrum inversion results for SAR data with 0° azimuth angle.
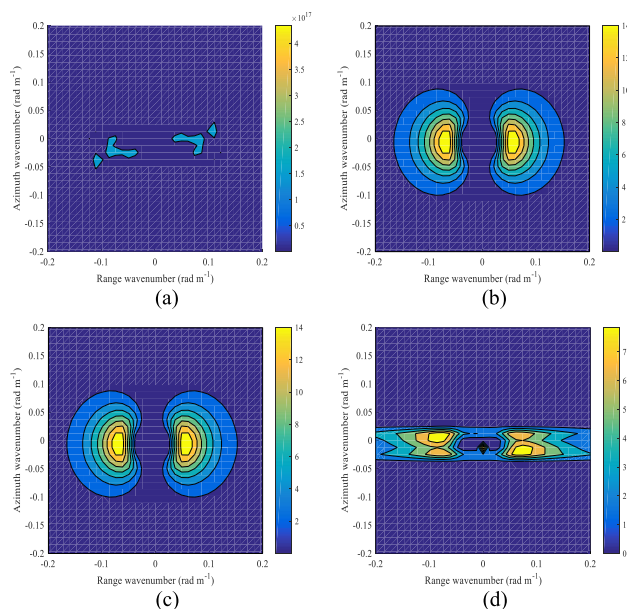

FIGURE 14. Wave spectrum inversion results for SAR data with azimuth angle of 90°.

The results before and after fusion are shown in Figure 15.

$$WS_{df} = \frac{45 \cdot WS_1}{180} + \frac{55 \cdot WS_2}{180} + \frac{65 \cdot WS_3}{180} \quad (18)$$

In equation (18), WS_1, WS_2, and WS_3 represent the wave spectra obtained from the single-SAR data inversion, and WS_{df} represents the wave spectrum after data fusion.

The azimuth cutoff compensation is ultimately verified by evaluating the significant wave height and the mean wave period. That is, it is generally considered that the root mean square error between the true value and the inversion value of the significant wave height should be less than 0.5 m. A root
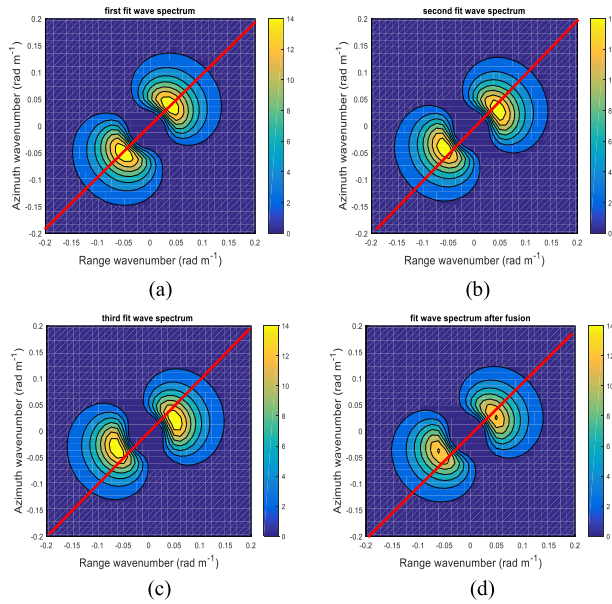
FIGURE 15. (a), (b), and (c) Optimal wave spectra for three groups of SAR data, and (d) optimal wave spectrum after data fusion.

mean square error of the mean wave period below 1.2 s is the index requirement in the field of ocean wave observation. To evaluate the accuracy of the inversion wave parameters, the true significant wave height is estimated using the wind speed as follows:

$$H_s = 0.0214 \cdot U_{19.5}^2, \quad (19)$$

where $U_{19.5}$ represents the wind speed at 19.5 m above sea level. However, the wind speed at 10 m above the sea surface is usually used for wave calculations. The conversion between these wind speeds is shown in equation (20) [24]:

$$U_h = U_{10} \cdot (1 + 2.5 \lg(\frac{h}{10})$$
$$(\sqrt{0.0015/[1 + \exp\left(-\frac{U_{10} - 1.25}{1.56}\right)] + 0.00104)}). \quad (20)$$

The significant wave height is inverted using equation (21). The wave spectrum corresponds to the optimum wave spectrum obtained by the MPI method.

$$H_s = 4\sqrt{m_0} = 4\sqrt{\int_0^\infty \int_0^\infty S(k_x, k_y) \mathrm{d}k_x \mathrm{d}k_y} \quad (21)$$

The calculation of the mean wave period (true value) is based on the significant wave period, which is calculated from the significant wave height. The mean wave period is related to the significant wave height using the relationship between the significant wave period and the mean wave period shown in equations (22)-(24).

$$\frac{gT_s}{2\pi U_{10}} = 3.31(\frac{gH_s}{U_{10}^2})^{\frac{3}{5}} \quad (22)$$

$$T_m = 0.74T_s \quad (23)$$

$$T_m = \frac{2\pi U_{10}}{g} \cdot 2.45 \cdot (\frac{gH_s}{U_{10}^2})^{\frac{3}{5}} \quad (24)$$

TABLE 5. Comparison of wave parameters before and after data fusion.

Optimal wave spectrum	SAR-1	SAR-2	SAR-3	After data fusion
Azimuth cutoff (m)	156.95	158.56	159.96	146.37
Input significant wave height (m)	2.27			
Inversion of significant wave height (m)	2.41			2.24
Input mean wave period (s)	6.15			
Inversion of mean wave period (s)	5.40			5.56

The inverted average wave period is calculated using the following formula [33]:

$$T_m = 2\pi \sqrt{\frac{m_0}{m_2}}$$
$$= 2\pi \sqrt{\frac{\int_0^\infty \int_0^\infty S(k_x, k_y) \mathrm{d}k_x \mathrm{d}k_y}{\int_0^\infty \int_0^\infty g\sqrt{k_x^2 + k_y^2} \cdot S(k_x, k_y) \mathrm{d}k_x \mathrm{d}k_y}}. \quad (25)$$

The azimuth cutoff, the significant wave height, and the mean wave period before and after data fusion are shown in Table 5. The initial input conditions, the significant wave height, and the mean wave period were the same for the three groups of SAR data. The azimuth cutoff after data fusion was smaller than that before fusion, showing that more complete wave information observed by SAR was obtained after fusion. Compared with the input, the biases of the significant wave height and the mean wave period were 0.14 m and 0.75 s, respectively, before data fusion and 0.03 m and 0.59 s, respectively, after data fusion. The significant wave height and the mean wave period after fusion were closer to the input values after fusion than before fusion. Compared to the prefusion results, fusion reduced the azimuth cutoff by 7.65%.

As the azimuth angles of the second group summed 225°, the fusion weights were set as the ratios between the azimuth angles and 270°. The fusion formula is given below, and the results before and after fusion are shown in Figure 16.

$$WS_{df2} = \frac{65 \cdot WS_3}{270} + \frac{75 \cdot WS_4}{270} + \frac{85 \cdot WS_5}{270} \quad (26)$$

In equation (26), WS_3, WS_4, and WS_5 represent the wave spectra of the second set of SAR data, and WS_{df2} represents the wave spectrum after data fusion.

The azimuth cutoff, the significant wave height, and the mean wave period before and after data fusion of the second group are shown in Table 6. Compared with the input, after data fusion, the biases of the significant wave height and the mean wave period were 0.09 m and 0.58 s, respectively. The azimuth cutoff after fusion was 11.89% lower than that before fusion.

The azimuth angles of the third group summed to 315°, and the azimuths were inversely proportional to the truncated wavelength. The fusion formula is given below, and the results before and after fusion are shown in Figure 17.

$$WS_{df3} = \frac{115 \cdot WS_6}{360} + \frac{105 \cdot WS_7}{360} + \frac{95 \cdot WS_8}{360} \quad (27)$$
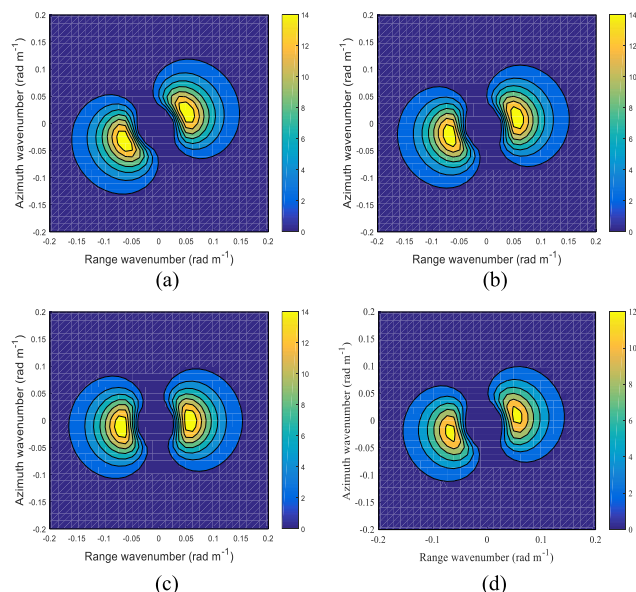
FIGURE 16. Fitted relationship between azimuth cutoff and wind speed for second data group.

TABLE 6. Comparison of wave parameters before and after data fusion.

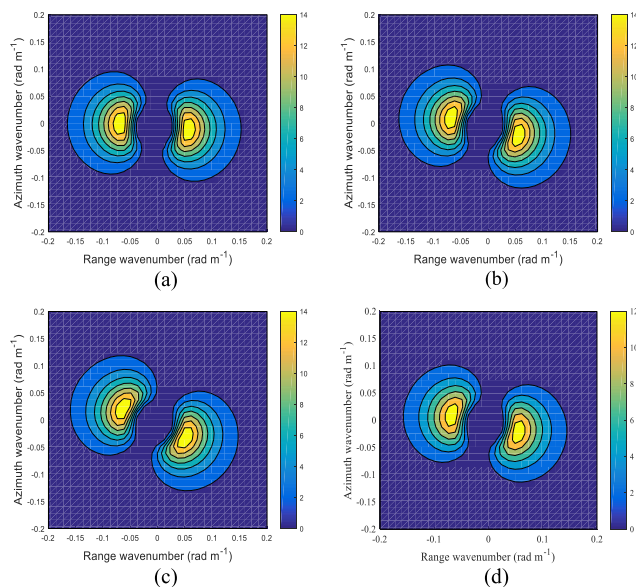| Optimal wave spectrum	SAR-1	SAR-2	SAR-3	After data fusion
Azimuth cutoff (m)	159.96	160.99	161.54	141.71
Input significant wave height (m)	2.27			
Inversion of significant wave height (m)	2.41			2.18
Input mean wave period (s)	6.15			
Inversion of mean wave period (s)	5.40			5.57

FIGURE 17. Fitted relationship between azimuth cutoff and wind speed for third data group.

In equation (27), WS_6, WS_7, and WS_8 represent the wave spectra of the third group, and WS_{df3} represents the wave spectrum after data fusion.

TABLE 7. Comparison of wave parameters before and after data fusion.

Optimal wave spectrum	SAR-1	SAR-2	SAR-3	After data fusion
Azimuth cutoff (m)	161.54	160.99	159.96	145.16
Input significant wave height (m)	2.27			
Inversion of significant wave height (m)	2.41			2.23
Input mean wave period (s)	6.15			
Inversion of mean wave period (s)	5.40			5.57

The azimuth cutoff, the significant wave height, and the mean wave period before and after data fusion for the third group are shown in Table 7. Compared with the input, after data fusion, the biases of the significant wave height and the mean wave period were 0.04 m and 0.58 s, respectively. The azimuth cutoff after fusion was 9.74% lower than that before fusion.

The results above show that the azimuth cutoff after data fusion was smaller than that before fusion. The significant wave height and mean wave period obtained after fusion were closer to the input value than before fusion, showing that more wave information by SAR and more accurate results were obtained after fusion. The following results were obtained considering all three groups. Fusion decreased the azimuth cutoff by 9.76% on average, the RMSE of the significant wave height is 0.06m, and the RMSE of the mean wave period is 0.58s. Thus, the proposed multiview wave spectrum data fusion method was effective for azimuth cutoff compensation.

The above results prove the effectiveness of the azimuth cutoff compensation method. This method has three main stages: generation of multiview SAR wave synchronization data, wave spectrum inversion, and data fusion. Wave spectrum inversion is an important step in the process of azimuth cutoff compensation. The applicability of the MPI algorithm to wave spectrum inversion was evaluated. We simulated SAR data in different wind speed ranges (5-29 m/s at 2 m/s-intervals), using an input E spectrum. The significant wave height was calculated from the wave spectrum. The significant wave height before and after inversion was used to evaluate the MPI inversion accuracy. In the wave inversion field, an error below 0.5 m indicates a high inversion accuracy.

The following conclusions were drawn from the calculation results. The error was relatively small for wind speeds of 5 m/s-15 m/s. The evaluation standard is that the error be less than 0.5 m, which is also a recognized standard in the field of remote sensing. For wind speeds above 15 m/s, the error gradually increased with the wind speed. Thus, the MPI method, and therefore the proposed method, are mainly applicable for wave spectrum and wave parameter inversion for low and medium sea states. Specifics of the calculation process have not been presented because of the large number of figures for wave spectrum inversion.

V. CONCLUSION
Multiview SAR wave synchronization data were used to analyze the influencing factors and compensation

methods for azimuth cutoff. The following conclusions can be drawn.

(1) In this study, the time-domain echo algorithm was used to calculate ocean surface echo signals. A large amount of computation was required, but the obtained SAR data had a high precision. The MPI inversion results demonstrated that the method was effective.

(2) When different wave parameters affected the azimuth cutoff, the relationship between the azimuth angle and the azimuth cutoff could not be derived from the real measured SAR data. The wind speed and the significant wave height were consistent for the simulation SAR wave data. The azimuth cutoff for each simulated SAR datum was calculated. The azimuth cutoff was then correlated with the azimuth angle. For acute (obtuse) azimuth angles, the azimuth cutoff wavelengths were proportional (inversely proportional) to the azimuth angles.

(3) Fusion of the wave spectrum data produced a significant wave height and mean wave period that were closer to the input values than those of the unfused wave spectrum. Fusion decreased the azimuth cutoff by 9.76% on average, the RMSE of the significant wave height is 0.06m, and the RMSE of the mean wave period is 0.58s. These results met the requirements of the observation index, indicating that the proposed azimuth cutoff compensation method was effective.

This study was based on simulation data, and verification using real measured data is planned for the future. The cooperative unit of the project has successfully developed SAR satellites and SAR airborne flight tests are planned to perform experiments with different observation directions in the same ocean area. This approach is expected to produce quasi-synchronized multiview SAR measured data and verify the azimuth cutoff wavelength compensation method. We also plan to determine the number of SAR satellites and angles required to optimize the azimuth cutoff compensation in satellite networking, which will help relevant agencies operating small SAR satellite networking launches to determine satellite orbit parameters.

REFERENCES

[1] K. Hasselmann and S. Hasselmann, "On the nonlinear mapping of an ocean wave spectrum into a synthetic aperture radar image spectrum and its inversion," *J. Geophys. Res.*, vol. 96, no. C6, p. 10713, 1991.

[2] W. Huang, X. Liu, and E. Gill, "Ocean wind and wave measurements using X-Band marine radar: A comprehensive review," *Remote Sens.*, vol. 9, no. 12, p. 1261, Dec. 2017.

[3] J. An, W. Huang, and E. W. Gill, "A self-adaptive wavelet-based algorithm for wave measurement using nautical radar," *IEEE Trans. Geosci. Remote Sens.*, vol. 53, no. 1, pp. 567–577, Jan. 2015.

[4] M. Bruck and S. Lehner, "Sea state measurements from TS-X SAR data," in *Proc. Terrasar Meeting*, 2011, pp. 1–5.

[5] W. Alpers, "Theory of radar imaging of internal waves," *Nature*, vol. 314, no. 6008, pp. 245–247, 1985.

[6] K. Hasselmann, "Theory of synthetic aperture radar ocean imaging: A MARSEN view," *J. Geophys. Res. Oceans*, vol. 90, no. C3, pp. 4659–4686, May 1985.

[7] X. Chen and W. Huang, "Identification of rain and low-backscatter regions in X-Band marine radar images: An unsupervised approach," *IEEE Trans. Geosci. Remote Sens.*, vol. 58, no. 6, pp. 4225–4236, Jun. 2020.

[8] X. Chen, W. Huang, C. Zhao, and Y. Tian, "Rain detection from X-band marine radar images: A support vector machine-based approach," *IEEE Trans. Geosci. Remote Sens.*, vol. 58, no. 3, pp. 2115–2123, Feb. 2020.

[9] P. W. Vachon, H. E. Krogstad, and J. S. Paterson, "Airborne and spaceborne synthetic aperture radar observations of ocean waves," *Atmosphere-Ocean*, vol. 32, no. 1, pp. 83–112, Mar. 1994.

[10] V. Kerbaol, B. Chapron, T. El Fouhaily, and R. Garello, "Fetch and wind dependence of SAR azimuth cutoff and higher order statistics in a mistral wind case," in *Proc. Int. Geosci. Remote Sens. Symp.*, May 1996, pp. 621–624.

[11] M. Marghany, Z. Ibrahim, and J. V. Genderen, "Azimuth cut-off model for significant wave height investigation along coastal water of Kuala Terengganu, Malaysia," *Int. J. Appl. Earth Observ. Geoinfor.*, vol. 4, no. 2, p. 160, 2002.

[12] R. Lin, J. Yang, G. Zheng, and J. Wang, "The significant wave height estimation by the azimuth cutoff of the quad-polarization SAR image," *Proc. SPIE Ocean Remote Sens. Monit. Space*, vol. 9261, Dec. 2014, Art. no. 926115.

[13] J. E. Stopa, F. Ardhuin, and B. Chapron, "Estimating wave orbital velocity through the azimuth cutoff from space-borne satellites," *J. Geophys. Res Oceans*, vol. 120, no. 11, pp. 7616–7634, 2015.

[14] G. Grieco, W. Lin, M. Migliaccio, F. Nirchio, and M. Portabella, "Dependency of the Sentinel-1 azimuth wavelength cut-off on significant wave height and wind speed," *Int. J. Remote Sens.*, vol. 37, no. 21, pp. 5086–5104, Nov. 2016.

[15] V. Corcione, G. Grieco, M. Portabella, F. Nunziata, and M. Migliaccio, "A novel azimuth cutoff implementation to retrieve sea surface wind speed from SAR imagery," *IEEE Trans. Geosci. Remote Sens*, vol. 57, no. 6, pp. 3331–3340, Jun. 2018.

[16] H. Li, A. Mouche, H. Wang, J. E. Stopa, and B. Chapron, "Polarization dependence of azimuth cutoff from quad-pol SAR images," *IEEE Trans. Geosci. Remote Sens.*, vol. 57, no. 12, pp. 9878–9887, Dec. 2019.

[17] D. R. Lyzenga and N. P. Malinas, "Azimuth falloff effects in two-antenna SAR measurements of ocean wave spectra," *IEEE Trans. Geosci. Remote Sens.*, vol. 34, no. 4, pp. 1020–1028, Jul. 1996.

[18] G. Franceschetti, M. Migliaccio, and D. Riccio, "On ocean SAR raw signal simulation," *IEEE Trans. Geosci. Remote Sens.*, vol. 36, no. 1, pp. 84–100, Oct. 1998.

[19] S. Hasselmann, C. Brüning, K. Hasselmann, and P. Heimbach, "An improved algorithm for the retrieval of ocean wave spectra from synthetic aperture radar image spectra," *J. Geophys. Res., Oceans*, vol. 101, no. C7, pp. 16615–16629, Jul. 1996.

[20] Y. Wan, X. Zhang, Y. Dai, and X. Shi, "Research on a method for simulating multiview ocean wave synchronization data by networked SAR satellites," *J. Mar. Sci. Eng.*, vol. 7, no. 6, p. 180, Jun. 2019.

[21] Y. Wan, X. Zhang, Y. Dai, and X. Shi, "An azimuth cut-off wavelength compensation method based on multiview synthetic aperture radar synchronization data," *Remote Sens. Lett.*, vol. 11, no. 3, pp. 245–254, Mar. 2020.

[22] T. Elfouhaily, "A unified directional spectrum for long and short wind-driven waves," *J. Geophys. Res*, vol. 102, no. C7, p. 15781, 1997.

[23] O. M. Phillips, "Spectral and statistical properties of the equilibrium range in wind-generated gravity waves," *J. Fluid Mech.*, vol. 156, pp. 505–531, 1985.

[24] X. J. Xu and X. F. Li, *Radar Phenomenological Models for Ships on Time-Evolving Sea Surface*. Beijing, China: National Defense Industry Press, 2013, pp. 29–30.

[25] V. Kudryavtsev, D. Akimov, J. Johannessen, and B. Chapron, "On radar imaging of current features: 1. Model and comparison with observations," *J. Geophys. Res.*, vol. 110, no. C07016, pp. 1–27, 2005.

[26] T. Yoshida and C.-K. Rheem, "SAR image simulation in the time domain for moving ocean surfaces," *Sensors*, vol. 13, no. 4, pp. 4450–4467, Apr. 2013.

[27] D. Lyzenga, "Numerical simulation of synthetic aperture radar image spectra for ocean waves," *IEEE Trans. Geosci. Remote Sens.*, vols. GE–24, no. 6, pp. 863–872, Nov. 1986.

[28] V. Kerbaol, B. Chapron, and P. W. Vachon, "Analysis of ERS-1/2 synthetic aperture radar wave mode imagettes," *J. Geophys. Res*, vol. 103, no. C4, p. 7833, 1998.

[29] A. L. Pleskachevsky, W. Rosenthal, and S. Lehner, "Meteo-marine parameters for highly variable environment in coastal regions from satellite radar images," *ISPRS J. Photogramm. Remote Sens.*, vol. 119, pp. 464–484, Sep. 2016.

[30] C. Brüning, W. Alpers, and K. Hasselmann, "Monte-carlo simulation studies of the nonlinear imaging of a two dimensional surface wave field by a synthetic aperture radar," *Int. J. Remote Sens.*, vol. 11, no. 10, pp. 1695–1727, Oct. 1990.

[31] K. Ward, "Sea clutter: Scattering, the *K* distribution and radar performance," *IET*, vol. 17, no. 2, pp. 233–234, 2013.

[32] T. Yoshida, "Azimuthal ocean wave emerged in SAR image spectra under specific condition," *J. Geophys. Res., Oceans*, vol. 122, no. 12, pp. 9625–9635, Dec. 2017.

[33] H. Wang, J. Zhu, J. Yang, and C. Shi, "A semiempirical algorithm for SAR wave height retrieval and its validation using Envisat ASAR wave mode data," *Acta Oceanologica Sinica*, vol. 31, no. 3, pp. 59–66, May 2012.

YONG WAN received the B.S. degree in application electronic technology and the M.S. degree in control theory and control engineering from the China University of Petroleum, Dongying, China, in 2001 and 2004, respectively, and the Ph.D. degree in marine information detection and processing from the Ocean University of China, Qingdao, China, in 2015.

Since 2019, he has been an Associate Professor with the China University of Petroleum, Qingdao. His research interests include marine information detection and processing, SAR detection for ocean wave and wind, wave energy, and wind energy assessment.

XIAOYU ZHANG received the bachelor's degree from Yantai University, Yantai, China, in 2017. She is currently pursuing the master's degree with the China University of Petroleum. Her research interests include marine information detection and processing and SAR detection for ocean wave.

YONGSHOU DAI received the B.S. degree in automation professional from the China University of Petroleum, Dongying, China, in 1986, the M.S. degree in computer application from Northern Jiaotong University, Beijing, China, in 1992, and the Ph.D. degree in control theory and control engineering from the University of Science and Technology Beijing, Beijing, in 2007. He is currently engaged in the teaching and research of marine information detection and processing at the College of Information and Control Engineering, China University of Petroleum, Qingdao, China.

LIGANG LI received the B.S. degree in industrial instrument automation and the M.S. degree in control theory and control engineering from the China University of Petroleum, Dongying, China, in 1998 and 2003, respectively, and the Ph.D. degree in control science and engineering from the University of Science and Technology Beijing, Beijing, China, in 2014.

He is currently an Associate Professor with the College of Ocean and Space Information, China University of Petroleum, Qingdao, China. His current research interests include USV intelligent control, obstacle detection, and intelligent information processing.

XIAOJUN QU received the Ph.D. degree from the College of Electronic Information and Control Engineering, Beijing University of Technology, Beijing, China, in 2015. He joined the China University of Petroleum, in 2003, where he is currently a Lecturer with the College of Information and Control Engineering. His current research interests include wave spectrometer, hybrid and network dynamic systems, and stability and consensus in networked multiagent systems.

• • •